Chapter 36
Influence of Free Volumes on Functional Properties of Modified Chalcogenide Glasses and Oxide Ceramics

H. Klym, O. Shpotyuk, A. Ingram, L. Calvez, I. Hadzaman, Yu. Kostiv, A. Ivanusa, and D. Chalyy

36.1 Introduction

An important area of electronic technology is the use of physical phenomena on nano- and subnanometer levels of structural organization of functional materials [1–3]. Transformation to these levels is achieved due to nanostructurization, i.e., formation of nanoobjects with the individual components (atoms or molecules) by their agglomeration or massive dissociation into individual components [4, 5]. In the case of disordered solids with full or partial absence of atomic structural correlations and excess free-volume configuration entropy or enthalpy, these processes occur in transformation of atom and void structures.

H. Klym (✉) • Y. Kostiv
Lviv Polytechnic National University, S. Bandery Str., 12, 79013, Lviv, Ukraine
e-mail: halyna.i.klym@lpnu.ua

O. Shpotyuk
Vlokh Institute of Physical Optics, 23, Dragomanov Str, 79005, Lviv, Ukraine

Jan Dlugosz University in Czestochowa, 13/15, Armii Krajowej Str., 42200, Czestochowa, Poland

A. Ingram
Opole University of Technology, Ozimska Str., 75, 45370, Opole, Poland

L. Calvez
Equipe Verres et et Céramiques, UMR-CNRS 6226, Institute des Sciences chimiques de Rennes, Université de Rennes 1, 35042, Rennes Cedex, France

I. Hadzaman
Drohobych State Pedagogical University, I. Franko Str., 24, 82100, Drohobych, Ukraine

A. Ivanusa • D. Chalyy
Lviv State University of Life Safety, Kleparivska Str., 35, 79000, Lviv, Ukraine

© Springer International Publishing AG 2017

O. Fesenko, L. Yatsenko (eds.), *Nanophysics, Nanomaterials, Interface Studies, and Applications*, Springer Proceedings in Physics 195,
DOI 10.1007/978-3-319-56422-7_36

From the standpoint of modern electronic technology, structural disordering is the basis of efficient and controlled process of obtaining various functional materials and flexible management of their functional properties due to reliable, efficient, and predictable physical and technological modifications, the possibility of additional pre- and post-process optimization processes [6–8]. Typical representatives of such materials are glasses and ceramics [9–12]. The structural disordering of these materials is impossible without the stabilization process of inner free volume. In addition, their functionality is closely related to nanostructurization under technological modifications and external factors.

An important role is void structure in chalcogenide glasses (ChG) which have a network structure with saturated covalent chemical bonds [13, 14]. Modern chalcogenide photonics [15] requires modification of disordered materials to ensure their functionality in a wide spectral range, which covers the area in both IR atmospheric windows and space telecommunications window [16]. Such modification of ChG is performed by injection of addition components (halide, metal activators, rare earth ions, etc.) into base matrix that destroy their network structure making local heterogeneity at nanolevel [17, 18]. This process is accompanied by not only the evolution of the atomic subsystem of glass materials but also the relevant changes in inner free-volume structure. Such modifications are characteristic for glass-ceramics due to process of controlled ceramization (i.e., formation of the inner structure of grains, pores, and grain boundaries) and functional ceramics for temperature- and umidity-sensitive elements [19, 20]. The main feature that combines ChG and oxide ceramics is disordering caused by nanostructurization of their inner free volumes.

The aim of this work is the investigation of inner free-volume structure and functional properties of row functional materials (chalcogenide $GeSe_2$-Ga_2Se_3 and GeS_2-Ga_2S_3-CsCl glasses as well as oxide $Cu_{0.4}Co_{0.4}Ni_{0.4}Mn_{1.8}O_4$ and MgO-Al_2O_3 ceramics) caused by their modifications.

36.2 Preparation of Glasses and Ceramics

The $80GeSe_2$-$20Ga_2Se_3$ chalcogenide glasses were prepared from highly pure raw materials Ge, Ga, and Se (99.999%) [18, 21, 22]. The materials were heated from 20 to 850 °C using 2 °C/min rate. Then, the silica tube was quenched in water at room temperature, annealed at 30 °C below the glass transition temperature (T_g = 370 °C) for 3 h, and finally slowly cooled down to room temperature [18]. The crystallization of the $80GeSe_2$-$20Ga_2Se_3$ ChG was performed at optimal temperature of ceramization (T_g + 10 °C) [21–23]. Thus, glass samples were placed in a ventilated furnace where the accuracy of temperature is ±2 °C for 25 and 50 h.

The GeS_2-Ga_2S_3-CsCl ChG were sintered from Ge, Ga, S, and CsCl compounds, as described in details elsewhere [24–26]. The glass transition temperatures T_g are 442 and 396 °C for $(80GeS_2\text{-}20Ga_2S_3)_{100-x}(CsCl)_x$, $x = 0$ and $x = 10$ glasses,

respectively [24, 26]. The obtained $(80GeS_2\text{-}20Ga_2S_3)_{100}(CsCl)_0$ and $(80GeS_2\text{-}20Ga_2S_3)_{90}(CsCl)_{10}$ glasses are referred as $(CsCl)_0$ and $(CsCl)_{10}$, respectively.

The $Cu_{0.1}Ni_{0.8}Co_{0.2}Mn_{1.9}O_4$ ceramics were prepared from high purity carbonate salts [27–29]. The mixture was thermally decomposed in the air at 700 ± 5 °C for 4 h. The prepared blanks were sintered in the air with respect to special time-temperature regimes, as described in details elsewhere [30–32]. It should be noted that the sintering route of ceramics was performed to ensure necessary conditions for inhibition effect in degradation [29, 33], the content of additional NiO phase with NaCl-type structure having decisive role in the final ceramics structure. The $Cu_{0.1}Ni_{0.8}Co_{0.2}Mn_{1.9}O_4$ ceramics with 1% and 8% NiO phase were prepared owing to different amounts of thermal energy transferred during the sintering [27, 29].

The $MgO\text{-}Al_2O_3$ ceramics were sintered at maximal temperature (T_s) 1300 °C for 2 h, as it was described elsewhere [34–36]. With respect to X-ray diffraction measurements [36], the ceramics contain main spinel and additional MgO (3.5%) phases.

36.3 Experimental Details

The PAL spectra for ChG and oxide ceramics were measured using ORTEC system of 230 ps resolution at the temperature $T = 22$ °C and relative humidity RH = 35% [21, 22, 35, 37]. For $MgO\text{-}Al_2O_3$ ceramics, PAL measurements were performed after initial drying, 7 days of water exposure (water vapor in desiccator at RH = 100%), and further final drying in a vacuum at 120 °C for 4 h [35]. Isotope ^{22}Na of slow activity (∼50 kBq) sandwiched between two identical tested samples was used as a source of positrons.

Each spectrum was measured with a channel width of 6.15 ps (the total number of channels was 8000) and contained at least $\sim 10^6$ coincidences in a total, which can be considered as conditions of normal PAL measurement statistics. To obtain data on longest-lived PAL components for $MgO\text{-}Al_2O_3$ ceramics, these ceramics were studied within a channel width of 61.5 ps [35]. The measured PAL spectra of glasses and ceramics were processed with standard LT 9.0 computer program [38]. The obtained curves were fitted by two components with lifetimes τ_1 and τ_2 and intensities I_1 and I_2 for $Cu_{0.1}Ni_{0.8}Co_{0.2}Mn_{1.9}O_4$ ceramics [39]; by three components with lifetimes τ_1, τ_2, and intensities τ_3 and I_1, I_2, and I_3 for $80GeSe_2\text{-}20Ga_2Se_3$ and $(80GeS_2\text{-}20Ga_2S_3)_{100}(CsCl)_0$ ($x = 0$ and $x = 10$) glasses [22, 25, 26]; and by four components with lifetimes τ_1, τ_2, τ_3, and τ_4 and intensities I_1, I_2, I_3, and I_4 for $MgO\text{-}Al_2O_3$ ceramics [34, 35].

The positron trapping modes in the studied samples such as average positron lifetimes τ_{av}, positron lifetime in defect-free bulk τ_b, positron trapping rate in defects κ_d, and fraction of trapped positrons η (for $80GeSe_2\text{-}20Ga_2Se_3$ glasses) were calculated using a formalism of two-state trapping model [21, 40, 41].

Optical transmission spectra of ChG were measured by Shimadzu UV-3600 spectrophotometer operated at room temperature in the visible and near-IR spectral region [21, 26, 42].

The humidity sensitivity of $MgO\text{-}Al_2O_3$ ceramics was determined by dependence of electrical resistance *R* on relative humidity *RH* of environment. The electrical resistance of the studied spinel ceramics was measured in the heat and humidity chamber PR-3E "TABAI" at 20 °C for *RH* in range 31–96% [34, 36]. The electrodes were attached to the connecting cables of M ohmmeter working at the fixed frequency of 500 Hz. The maximal overall uncertainties in the electrical measurements did not exceed approximately ±(0.02–0.04) MOhm in electrical resistance. The confidence interval in *RH* measuring bar restricted by equipment accuracy was no worse than ±1% [36].

The degradation tests for $Cu_{0.1}Ni_{0.8}Co_{0.2}Mn_{1.9}O_4$ ceramics were performed at temperature of 170 °C lasting defined time intervals (within 10 time domains from 24 to 500 h) [27, 29, 33]. The results of aging tests were controlled by relative resistance drift (*RRD*) defined as changes in electrical resistance $\Delta R/R_0$ measured in the normal conditions (near 25 °C and 35% of relative humidity) using digital multimeter. The confidence interval in the *RRD* measuring error bar restricted by equipment inaccuracy was no worse than ±0.2%. The maximal overall uncertainties in the electrical measurements did not exceed approximately ±(0.4–0.5)% [27].

36.4 Results and Discussion

36.4.1 The Ge-Ga-Se Glasses Modified by Crystallization Process

With respect to XRD data, as it was noted earlier [21, 22], with increasing annealing time to 25 and 50 h at 380 °C, the well-pronounced crystalline peaks at $2\theta \sim 28°$ appear. The positions of these peaks are in agreement with $GeGa_4Se_8$ and Ga_2Se_3 phase indexation [22]. In fact, all principal XRD peaks of $GeGa_4Se_8$ and Ga_2Se_3 phases coincide, so we consider them in crystallized $80GeSe_2\text{-}20Ga_2Se_3$ glass as signatures of both these phases (Ga_2Se_3 and $GeGa_4Se_8$). The width of this peak ($2\theta \sim 28°$) confirms the presence of nanoparticles in a glassy matrix in the form of nanocrystallites with 9–10 nm in sizes [21].

The changes in the atomistic structure of $80GeSe_2\text{-}20Ga_2Se_3$ ChG from amorphous to crystallized one are accompanied by transformations in the void structure. The results of PAL measurements confirm such diversity of void evolution processes in the studied glasses. Fitting parameters and corresponding positron trapping modes for PAL spectra of $80GeSe_2\text{-}20Ga_2Se_3$ glasses are given in Table 36.1. As was described earlier in [22], the first component (τ_1, I_1) has no physical meaning for chalcogenide glasses. With respect to two-state positron trapping model for ChG [40], the τ_2 lifetime is directly related to the size of free volumes (trapping centers),

Table 36.1 Fitting parameters and positron trapping modes for PAL spectra of $80GeSe_2$-$20Ga_2Se_3$ glasses before (0 h) and after (25 h and 50 h) thermal annealing

Annealing duration	Fitting parameters					
	τ_1, ns	I_1, %	τ_2, ns	I_2, %	τ_3, ns	I_3, %
0 h	0.209	0.610	0.426	0.360	1.967	0.030
25 h	0.215	0.633	0.432	0.337	2.038	0.030
50 h	0.210	0.605	0.424	0.365	2.159	0.030
Annealing duration	Positron trapping modes					
	$\tau_{av.}$, ns	τ_b, ns	κ_d, ns	$\tau_2 - \tau_b$, ns	τ_2/τ_b	η
0 h	0.290	0.258	0.91	0.17	1.65	0.19
25 h	0.291	0.261	0.82	0.17	1.66	0.18
50 h	0.292	0.260	0.92	0.16	1.63	0.19

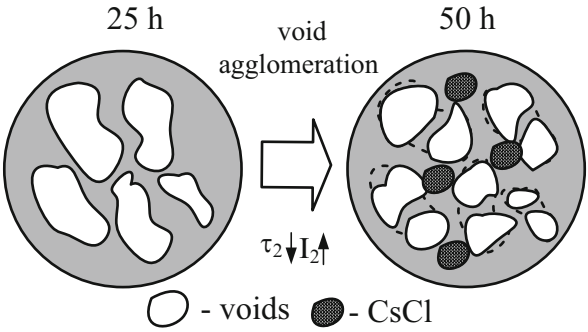

Fig. 36.1 Schematic illustration of free-volume void fragmentation during crystallization process in the $80GeSe_2$-$20Ga_2Se_3$ chalcogenide glasses caused by annealing from 25 to 50 h

and intensity I_2 is proportional to the number of such defects under condition of the same defect-free bulk annihilation lifetime. The third component (τ_3, I_3) in the fitting curves corresponds to ortho-positronium *o-Ps* formation on level of 3%.

With extending the annealing duration to 25 h, the lifetime τ_2 increases, and I_2 intensity decreases due to void agglomeration. This trend reduces the positron trapping rate κ_d without significant changes in $\tau_{av.}$ and τ_b lifetimes. With further extension of annealing duration to 50 h, the I_2 intensity increases, while lifetime τ_2 decreases to 0.424 ns. These changes result in increased positron trapping rate κ_d. Other positron trapping parameters such as τ_2/τ_b and η behave under annealing in line with these changes (Table 36.1). The fraction of trapped positrons η decreases in the initial stage of treatment to 25 h and increases at further annealing to 50 h.

During the crystallization process at annealing for 50 h, the glass structure relaxes toward more thermodynamically favorable state [22, 43]. It means that free-volume nanovoids can be essentially transformed in this process. In the case of the studied ChG, the fragmentation of larger free-volume entities into smaller ones occurs (Fig. 36.1). Such process is accompanied by a decrease in τ_2 lifetime and a corresponding increase in I_2 intensity.

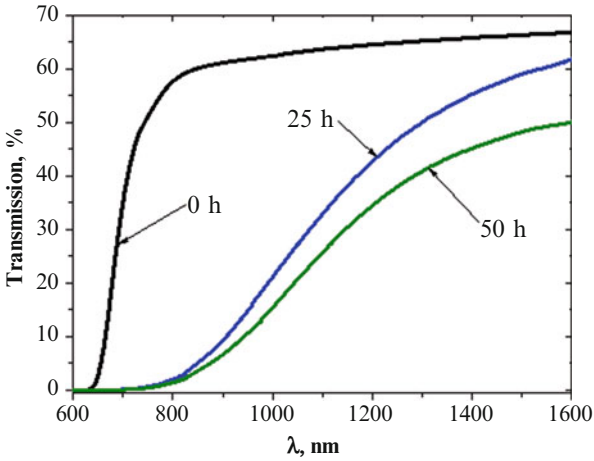

Fig. 36.2 Optical transmission spectra for $80GeSe_2$-$20Ga_2Se_3$ glass before (0 h) and after heat treatment times at 380 °C during 25 and 50 h

Thus, nearly the same τ_b and τ_{av} values are characteristic for all ChG samples, while the positron trapping rate in extended defects κ_d decreases with nucleation of crystallized phases (annealing for 25 h) and increases with crystallization (annealing at 50 h). The crystal growth is accompanied by network shrinkage of $80GeSe_2$-$20Ga_2Se_3$ glass, the agglomeration of free-volume voids occurring more rapidly than their appearance due to mismatch between growing crystallites and remainder of the glass matrix [21, 22].

The process of crystallization in the $80GeSe_2$-$20Ga_2Se_3$ glasses influences their functionality, i.e., optical transmission spectra. The non-annealed glassy samples (0 h) show maximum optical transmittance at the level of 65% (Fig. 36.2). Annealing at 380 °C for 25 and 50 h decreases this transmittance and shifts optical transmission edge toward long-wave side. The appearance of growing of Ga_2Se_3 and $GeGa_4Se_8$ nanocrystals inside glassy matrix induces light scattering at shorter wavelengths [21].

36.4.2 The Ge-Ga-S Glasses Modified by CsCl Additives

Fitting parameters and positron trapping modes calculated within three-component fitting procedure for PAL spectra of $(80GeS_2\text{-}20Ga_2S_3)_{100-x}(CsCl)_x$, ($0 = 0$, $x = 10$) glasses are given in Table 36.2. As was shown previously, the τ_2 lifetime shows the size of free voids where positrons are trapped, and the intensity I_2 is proportional to the number of these voids. The positronium trapping in the third component (τ_3, I_3) is estimated at the level of 1–3% [16, 25, 26]. We analyze the PAL results with respect to the second defect-related component (τ_2, I_2) reflecting

Table 36.2 Fitting parameters and positron trapping modes for PAL spectra of $(80GeS_2\text{-}20Ga_2S_3)_{100-x}(CsCl)_x$, $(0 = 0, x = 10)$ glasses

Sample	Fitting parameters						Positron trapping modes		
	τ_1, ns	I_1, a.u.	τ_2, ns	I_2, a.u.	τ_3, ns	I_3, a.u.	$\tau_{av.}$, ns	τ_b, ns	κ_d, ns^{-1}
$(CsCl)_0$	0.201	0.581	0.426	0.387	1.958	0.032	0.310	0.279	0.59
$(CsCl)_{10}$	0.249	0.696	0.499	0.290	2.029	0.014	0.313	0.282	0.73

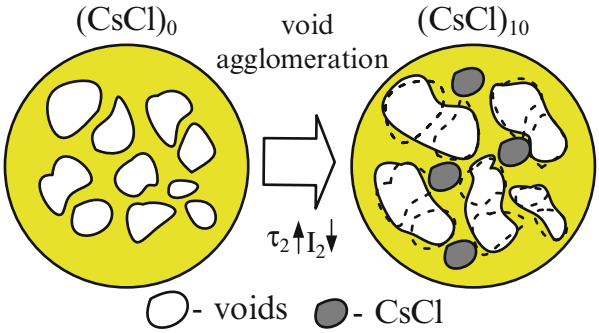

Fig. 36.3 Schematic illustration of free-volume void agglomeration in $(80GeS_2\text{-}20Ga_2S_3)_{100-x}(CsCl)_x$, $(0 = 0, x = 10)$ glasses

evolution of voids in GeS_2-Ga_2S_3-CsCl ChG caused by CsCl presence in the glass matrix. These nanovoids have the same meaning as atomic vacancies [23].

Thus, the lifetime τ_2 increases from 0.426 ns for $(CsCl)_0$ to 0.499 for $(CsCl)_{10}$ ChG samples, while the intensity I_2 decreases (Table 36.2). Consequently, positron trapping rate κ_d correlates with τ_2 and I_2 parameters and decreases due to the drop of the intensity I_2. Such changes of PAL parameters describe the agglomeration of free-volume nanovoids in the inner structure of ChG (Fig. 36.3). The positron trapping rate in defects κ_d increases from 0.59 ns^{-1} for $(CsCl)_0$ to 0.73 ns^{-1} in $(CsCl)_{10}$, and the density ρ of these glasses also increases with CsCl content [25, 26].

The CsCl additives in the base GeS_2-Ga_2S_3 glassy matrix have influence on their optical transmission spectra. The transmission in the visible region of spectra for studied ChG is shown in Fig. 36.4.

The $(CsCl)_0$ samples are essentially transparent down to 500 nm, and CsCl content in the glassy matrix results in the shift of the absorption edge toward shorter wavelengths (similar effect is described in [24, 25, 44]). The transmission increases with CsCl from 77% in $CsCl_0$ to 83% in $CsCl_{10}$. From a structural point of view, the addition of CsCl in GeS_2-Ga_2S_3 glasses is characterized by the formation of $GaS_{4-x}Cl_x$ tetrahedra that are dispersed in the glass network [24]. So, the average number of Ga-S bonds decreases for the benefit of the average number of Ga-Cl bonds.

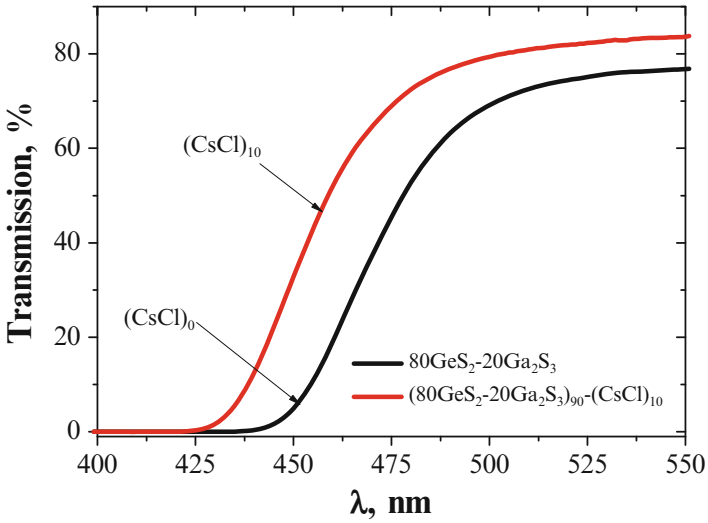

Fig. 36.4 Optical transmission spectra of $(80GeS_2\text{-}20Ga_2S_3)_{100-x}(CsCl)_x$ ($x = 0$ and $x = 10$) chalcogenide glasses

Table 36.3 Fitting parameters and positron trapping modes for PAL spectra of $Cu_{0.4}Co_{0.4}Ni_{0.4}Mn_{1.8}O_4$ ceramics mathematically treated within two-component fitting procedure

	Fitting parameters				Positron trapping modes		
NiO amount	τ_1, ns	I_1, a.u.	τ_2, ns	I_2, a.u.	$\tau_{av.}$, ns	τ_b, ns	κ_d, ns^{-1}
1% NiO	0.19	0.82	0.38	0.18	0.23	0.21	0.48
8% NiO	0.17	0.79	0.36	0.21	0.21	0.19	0.62

36.4.3 The $Cu_{0.1}Ni_{0.8}Co_{0.2}Mn_{1.9}O_4$ Ceramics Modified by NiO Phase

As was shown previously in [39], for oxide spinel-type ceramic materials, the first component of spectra was connected with main spinel structure and the second one with extended defects located near grain boundaries in the vicinity of additional extracted phases. The intensity I_1 corresponds to the amounts of the main spinel phase, while the I_2 intensity to the amount of additional NiO phase near grain boundaries.

The lifetime of the first and second components for $Cu_{0.1}Ni_{0.8}Co_{0.2}Mn_{1.9}O_4$ ceramics is typical for spinel-structured materials and equals 0.38 ns (Table 36.3). The lower τ_1 value in ceramics with 1% NiO (0.17 ns) is well correlated with this NiO content in different crystallographical positions. Since the amount of grain/pores in these samples was larger [45], the process of positron trapping in these ceramics was more intensive (the positron trapping rate of defects increased from 0.48 to 0.62 ns^{-1}).

The intensity of the second component for ceramics with 1% NiO is 0.18 a.u. This additional NiO phase is localized near grain boundaries and partly fills pores [45]. Then the intensity I_2 increases to 0.21 a.u. correspondingly to the increasing amount of NiO phase near grain boundaries and the size of defects increases (τ_2 reduces from 0.38 to 0.36 ns). These transformations were in good agreement with positron trapping parameters. Nevertheless, there were no significant changes in τ_{av} and τ_b parameters. In all cases, the same type of positron trapping center is formed [46].

The changes in microstructure of $Cu_{0.1}Ni_{0.8}Co_{0.2}Mn_{1.9}O_4$ ceramics are reflected in their stability in time (electronic relaxation kinetics). Kinetic curves illustrating the *RRD* defined by $\Delta R/R_0$ values in $Cu_{0.1}Ni_{0.8}Co_{0.2}Mn_{1.9}O_4$ ceramics with 1% and 8% NiO phase are shown in Fig. 36.5.

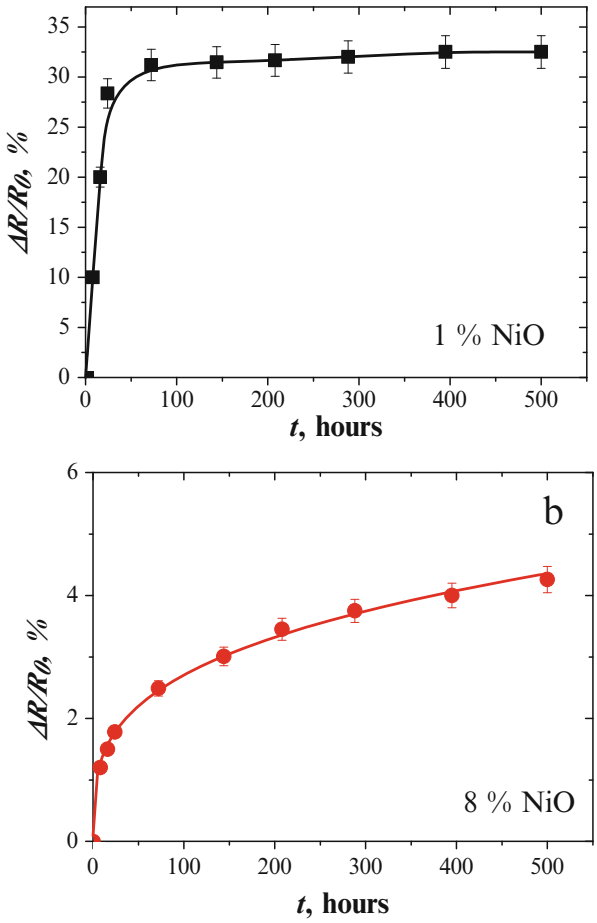

Fig. 36.5 The *RRD* ($\Delta R/R_0$) in $Cu_{0.1}Ni_{0.8}Co_{0.2}Mn_{1.9}O_4$ ceramics (**a** – 1% NiO; **b** – 8% NiO) caused by prolonged storage at 170 °C (with error bar data)

The ceramic samples with 1% NiO phase are characterized by the largest value of *RRD* reaching more than 30% (Fig. 36.5a). With the increase in the amount of NiO phase to 8%, the saturated *RRD* value decreased to 4.3% (Fig. 36.5b). Obviously, increasing of NiO amount is needed for stabilization of electrical parameters of these ceramics.

36.4.4 Water Vapor Sorption Processes in the $MgO\text{-}Al_2O_3$ Ceramics

As it was shown earlier [34–36, 47], the positron annihilation in humidity-sensitive $MgO\text{-}Al_2O_3$ ceramics is revealed through two different channels related to positron trapping (component with lifetime τ_2) and o-Ps decaying (two long-lived components with τ_3 and τ_4 lifetimes). The first component with parameters τ_1 and I_1 reflects mainly microstructure specificity of spinel ceramics along with input from annihilation of para-Ps atoms [34]. The lifetime τ_2 is related to the size of free-volume nanodefects near grain boundaries, and I_2 intensity reflects their amount [41]. The third and the fourth components (τ_3, I_3) and (τ_4, I_4) correspond to annihilation of *o-Ps* in intrinsic nanopores of $MgO\text{-}Al_2O_3$ ceramics [35, 48].

PAL parameters obtained within four-component treatment of the PAL spectra of initial, water-vapored, and dried $MgO\text{-}Al_2O_3$ ceramics sintered at 1300 °C are shown in Table 36.4.

Decreasing the lifetime τ_2 in water-vapored $MgO\text{-}Al_2O_3$ ceramics and increasing their intensity I_2 show intensification of positron trapping in defects near grain boundaries filled with water. After drying, the intensities I_2 almost completely return to the initial values (characteristic for initially dry samples). Thus, the water adsorption processes in $MgO\text{-}Al_2O_3$ ceramics are accompanied by fragmentation of positron trapping sites near grain boundaries, and, respectively, the water desorption processes are accompanied by agglomeration of free-volume voids.

Table 36.4 Fitting parameters and positron trapping modes for PAL spectra of $MgO\text{-}Al_2O_3$ ceramics sintered at 1300 °C obtained from four-component procedure

Sample	Fitting parameters							
	τ_1, ns	I_1, a.u.	τ_2, ns	I_2, a.u.	τ_3, ns	I_3, a.u.	τ_4, ns	I_4, a.u.
Initial	0.155	0.82	0.414	0.16	2.426	0.008	68.74	0.014
Water vapor	0.161	0.76	0.400	0.21	2.619	0.018	58.33	0.007
Drying	0.156	0.82	0.421	0.15	2.448	0.007	68.17	0.014
	Positron trapping modes						Pore radius	
	$\tau_{av.}$, ns		τ_b, ns		κ_d, ns^{-1}		R_3, nm	R_4, nm
Initial	0.197		0.17		0.66		0.325	1.818
Water vapor	0.213		0.19		0.80		0.340	1.630
Drying	0.198		0.17		0.63		0.327	1.807

Water vapor sorption processes in the studied $MgO\text{-}Al_2O_3$ ceramics result in essential evolution of the third and fourth *o-Ps*-related components. The intensity I_3 increases in initially dry samples after water vapor exposure, thus confirming *o-Ps* annihilation in water-filled nanopores through a "bubble" mechanism (with corresponding o-Ps lifetime close to 1.8 ns) [49–51]. After drying, the intensities of the third and fourth components return to the initial value, confirming high efficiency of water adsorption-desorption processes. The intensity I_4 decreases in water vapor exposed ceramics samples. After drying (in a vacuum at 120 °C for 4 h) of the ceramic samples previously exposed to water vapor, the initial pore size tends to be restored (Table 36.4).

Additionally, the radii R_3 and R_4 of spherical nanopores were calculated using *o-Ps*-related τ_3 and τ_4 lifetimes in known Tao-Eldrup model [52, 53]. The decreased τ_4 value for ceramics dried after water vapor exposure can be connected with formation of thin layers of water molecules covering the walls of pores with radii of 1.8 nm, which are not completely removed after vacuum annealing at 120 °C for 4 h.

Changes caused by inner nanoporous structure of $MgO\text{-}Al_2O_3$ ceramics were reflected in their humidity sensitivity. In spite of a small amount of transporting pores [34, 36, 53], ceramics are characterized by linear dependence of electrical resistance *R* vs. *RH* in the entire studied region (from 30% to 98% of *RH*) without significant hysteresis in absorption-desorption cycles (Fig. 36.6). Humidity sensitivity of ceramics sintered at 1300 °C results in increased amount of open water-exchange outside-delivering macropores [36]. They provide efficient sorption processes of water through small amount of communication mesopores.

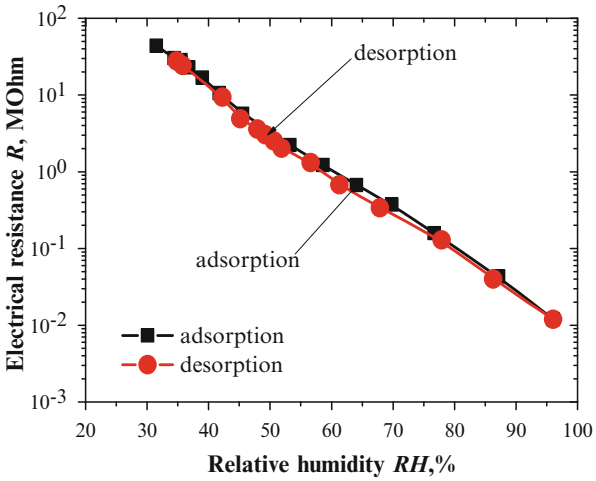

Fig. 36.6 Exploitation properties of $MgO\text{-}Al_2O_3$ ceramics sintered at 1300 °C in absorption-desorption cycle

36.5 Conclusions

Influences of inner free-volume structure on the functional properties of chalcogenide $GeSe_2$-Ga_2Se_3 and GeS_2-Ga_2S_3-CsCl glasses as well as oxide $Cu_{0.4}Co_{0.4}Ni_{0.4}Mn_{1.8}O_4$ and MgO-Al_2O_3 ceramics caused by their different modifications are investigated.

In the case of $80GeSe_2$-$20Ga_2Se_3$ glasses, it was shown that crystallization process during annealing at 380 °C for 25 and 50 h indicates specific fragmentation of larger free-volume nanovoids into a greater number of smaller ones. Annealing at 380 °C for 25 and 50 h results in the decreasing of transmittance and shifts optical transmission edge toward long-wavelength region.

For GeS_2-Ga_2S_3-CsCl ChG, it is established that CsCl additives transform free volume (void agglomeration in ChG with 10% mol. of CsCl) and optical properties of glass matrix. The shift of the absorption edge toward shorter wavelengths is observed in Ge-Ga-S ChG with CsCl content.

In $Cu_{0.1}Ni_{0.8}Co_{0.2}Mn_{1.9}O_4$ ceramics with 8% of NiO phase addition, positron trapping defects (or free volumes) near grain boundaries are formed. The character of thermally induced electronic degradation in structurally modified $Cu_{0.1}Ni_{0.8}Co_{0.2}Mn_{1.9}O_4$ ceramics shows stretched exponential behavior.

In modified MgO-Al_2O_3 ceramics sintered at 1300 °C, it is shown that drying of ceramics in vacuum at 120 °C previously exposed to water vapor does not restore initial pore size, confirming sensitivity of PAL method to amount of water molecules adsorbed in nanopores. The water vapor modifies defects in ceramics located near grain boundaries, and this process is accompanied by void fragmentation at water adsorption with further void agglomeration at water desorption after drying. Using lifetimes of the third and fourth components of PAL spectra, the radii of nanopores were calculated using Tao-Eldrup model. The MgO-Al_2O_3 ceramics sintered at 1300 °C are humidity sensitive from 30% to 98% of *RH*.

Acknowledgment H. Klym thanks the Ministry of Education and Science of Ukraine for the support (grant No 0116U004411).

References

1. Zhao X, Ren X, Sun C, Zhang X, Si Y, Yan C, Xu J, Xue D (2008) Morphology evolution at nano- to micro-scale. Funct Mater Lett 1(03):167–172. http://dx.doi.org/10.1142/S1793604708000393
2. Wilson SA, Jourdain RP, Zhang Q, Dorey RA, Bowen CR, Willander M, Al-hilli SM, Nur O, Quandt E, Johansson C, Pagounis E, Kohl M, Matovic J, Samel B, Wijngaart W, Jager EWH, Carlsson D, Djinovic Z, Wegener M, Moldovan C, Iosub R, Abad E, Wendlandt M, Rusu C, Persson K (2007) New materials for micro-scale sensors and actuators: an engineering review. Materials Science and Engineering: R: Reports 56(1):1–129. http://dx.doi.org/10.1016/j.mser.2007.03.001

3. Cain M, Morrell R (2001) Nanostructured ceramics: a review of their potential. Appl Organomet Chem 15(5):321–330. doi:10.1002/aoc.153
4. Dutta J, Hofmann H (2003) Nanomaterials. Swiss Federal Institute of Technology. Lausanne, pp 9–20
5. Gabor L, Hornyak JJ, Moore HF, Dutta J (2008) Fundamentals of nanotechnology. CRC Press, Boca Raton, p 786
6. Donth EJ (2013) The glass transition: relaxation dynamics in liquids and disordered materials, vol 48. Springer Science & Business Media, Berlin, p 418
7. Kierlik E, Monson PA, Rosinberg ML, Sarkisov L, Tarjus G (2001) Capillary condensation in disordered porous materials: hysteresis versus equilibrium behavior. Phys Rev Lett 87(5):055701. https://doi.org/10.1103/PhysRevLett.87.055701
8. Holand W, George H, Beall GH (2012) Glass ceramic technology. Wiley, Hoboken, p 440
9. Seddon AB (1995) Chalcogenide glasses: a review of their preparation, properties and applications. J Non-Cryst Solids 184:44–50. http://dx.doi.org/10.1016/0022-3093(94)00686-5
10. Zakery A, Elliott SR (2003) Optical properties and applications of chalcogenide glasses: a review. J Non-Cryst Solids 330(1):1–12. http://dx.doi.org/10.1016/j.jnoncrysol.2003.08.064
11. Li JG, Ikegami T, Lee JH, Mori T (2000) Fabrication of translucent magnesium aluminum spinel ceramics. J Am Ceram Soc 83(11):2866–2868. doi:10.1111/j.1151-2916.2000.tb01648.x
12. Dorey RA, Rocks S, Dauchy F, Navarro A (2006) New advances in forming functional ceramics for micro devices. Advances in Science and Technology 45:2440–2447. doi:10.4028/www.scientific.net/AST.45.2440
13. Zakery A, Elliott SR (2007) Optical switching in Chalcogenide glasses. In: Optical nonlinearities in chalcogenide glasses and their applications. Springer, Berlin/Heidelberg, pp 129–150. doi:10.1007/978-3-540-71068-4_6
14. Elliott SR (1977) A theory of ac conduction in chalcogenide glasses. Philos Mag 36(6):1291–1304. http://dx.doi.org/10.1080/14786437708238517
15. Eggleton BJ, Luther-Davies B, Richardson K (2011) Chalcogenide photonics. Nat Photonics 5(3):141–148. doi:10.1038/nphoton.2011.309
16. Klym H, Ingram A, Shpotyuk O (2016) Free-volume nanostructural transformation in crystallized GeS_2–Ga_2S_3–CsCl glasses. Mater Werkst 47(2–3):198–202. doi:10.1002/mawe.201600476
17. Ren J, Wagner T, Bartos M, Frumar M, Oswald J, Kincl M, Frumarova B, Chen G (2011) Intense near-infrared and midinfrared luminescence from the Dy^{3+}-doped $GeSe_2$–Ga_2Se_3–MI (M= K, Cs, Ag) chalcohalide glasses at 1.32, 1.73, and 2.67 μm. J Appl Phys 109(3):033105. http://dx.doi.org/10.1063/1.3531555
18. Calvez L, Lucas P, Rozé M, Ma HL, Lucas J, Zhang XH (2007) Influence of gallium and alkali halide addition on the optical and thermo-mechanical properties of $GeSe_2$-Ga_2Se_3 glass. Applied Physics A 89(1):183–188. doi:10.1007/s00339-007-4081-y
19. Arai H, Seiyama T (2008) Humidity sensors. In: Sensors set: a comprehensive survey. Wiley-VCH Verlag GmbH, Weinheim, pp 981–1012. doi:10.1002/9783527619269.ch7b
20. Fraden J (2004) Handbook of modern sensors: physics, designs, and applications. Springer Science & Business Media, Cham
21. Klym H, Ingram A, Shpotyuk O, Calvez L, Petracovschi E, Kulyk B, Serkiz R, Szatanik R (2015) 'Cold' crystallization in nanostructurized $80GeSe_2$-$20Ga_2Se_3$ glass. Nanoscale Res Lett 10(1):1–8. doi:10.1186/s11671-015-0775-9
22. Shpotyuk O, Calvez L, Petracovschi E, Klym H, Ingram A, Demchenko P (2014) Thermally-induced crystallization behaviour of $80GeSe_2$-$20Ga_2Se_3$ glass as probed by combined X-ray diffraction and PAL spectroscopy. J Alloys Compd 582:323–327. http://dx.doi.org/10.1016/j.jallcom.2013.07.127
23. Shpotyuk O, Filipecki J, Ingram A, Golovchak R, Vakiv M, Klym H, Balitska V, Shpotyuk M, Kozdras A (2015) Positronics of subnanometer atomistic imperfections in solids as a high-informative structure characterization tool. Nanoscale Res Lett 10(1):1–5. doi:10.1186/s11671-015-0764-z

24. Masselin P, Le Coq D, Calvez L, Petracovschi E, Lépine E, Bychkov E, Zhang X (2012) CsCl effect on the optical properties of the $80GeS_2$–$20Ga_2S_3$ base glass. Applied Physics A 106(3):697–702. doi:10.1007/s00339-011-6668-6
25. Klym H, Ingram A, Shpotyuk O, Karbovnyk I (2016) Influence of CsCl addition on the nanostructured voids and optical properties of 80GeS2-20Ga2S3 glasses. Opt Mater 59:39–42. http://dx.doi.org/10.1016/j.optmat.2016.03.004
26. Klym H, Ingram A, Shpotyuk O, Hotra O, Popov AI (2016) Positron trapping defects in free-volume investigation of Ge-Ga-S-CsCl glasses. Radiat Meas 90:117–121. http://dx.doi.org/10.1016/j.radmeas.2016.01.023
27. Shpotyuk O, Balitska V, Brunner M, Hadzaman I, Klym H (2015) Thermally-induced electronic relaxation in structurally-modified $Cu_{0.1}Ni_{0.8}Co_{0.2}Mn_{1.9}O_4$ spinel ceramics. Phys B Condens Matter 459:116–121. http://dx.doi.org/10.1016/j.physb.2014.11.023
28. Klym H, Hadzaman I, Shpotyuk O, Fu Q, Luo W, Deng J (2013) Integrated thick-film p-i-p+ structures based on spinel ceramics. Solid State Phenom 200:156–161. http://www.scientific.net/SSP.200.156
29. Klym H, Balitska V, Shpotyuk O, Hadzaman I (2014) Degradation transformation in spinel-type functional thick-film ceramic materials. Microelectron Reliab 54(12):2843–2848. http://dx.doi.org/10.1016/j.microrel.2014.07.137
30. Klym H, Hadzaman I, Ingram A, Shpotyuk O (2013) Multilayer thick-film structures based on spinel ceramics 1. Can J Phys 92(7/8):822–826. doi:10.1139/cjp-2013-0597
31. Klym H, Hadzaman I, Shpotyuk O, Brunner M (2014) Integrated thick-film nanostructures based on spinel ceramics. Nanoscale Res Lett 9(1):1–6. doi:10.1186/1556-276X-9-149
32. Vakiv M, Hadzaman I, Klym H, Shpotyuk O, Brunner M (2011) Multifunctional thick-film structures based on spinel ceramics for environment sensors. J Phys Conf Ser 289(1):012011. http://dx.doi.org/10.1088/1742-6596/289/1/012011
33. Shpotyuk O, Brunner M, Hadzaman I, Balitska V, Klym H (2016) Analytical description of degradation-relaxation transformations in nanoinhomogeneous spinel ceramics. Nanoscale Res Lett 11(1):499. doi:10.1186/s11671-016-1722-0
34. Klym H, Ingram A, Shpotyuk O, Hadzaman I, Hotra O, Kostiv Y (2016) Nanostructural free-volume effects in humidity-sensitive MgO-Al_2O_3 ceramics for sensor applications. J Mater Eng Perform 25(3):866–873. doi:10.1007/s11665-016-1931-9
35. Klym H, Ingram A, Shpotyuk O, Hadzaman I, Solntsev V (2016) Water-vapor sorption processes in nanoporous MgO-Al_2O_3 ceramics: the PAL spectroscopy study. Nanoscale Res Lett 11(1):1. doi:10.1186/s11671-016-1352-6
36. Klym H, Hadzaman I, Shpotyuk O (2015) Influence of sintering temperature on pore structure and electrical properties of technologically modified MgO-Al_2O_3 ceramics. Mater Sci 21(1):92–95. http://dx.doi.org/10.5755/j01.ms.21.1.5189
37. Karbovnyk I, Bolesta I, Rovetskii I, Velgosh S, Klym H (2014) Studies of CdI_2-Bi_3 microstructures with optical methods, atomic force microscopy and positron annihilation spectroscopy. Materials Science-Poland 32(3):391–395. doi:10.2478/s13536-014-0215-z
38. Kansy J (1996) Microcomputer program for analysis of positron annihilation lifetime spectra. Nucl Instrum Methods Phys Res, Sect A 374(2):235–244. http://dx.doi.org/10.1016/0168-9002(96)00075-7
39. Klym H, Ingram A, Shpotyuk O, Filipecki J, Hadzaman I (2011) Structural studies of spinel manganite ceramics with positron annihilation lifetime spectroscopy. J Phys Conf Ser 289(1):012010. http://iopscience.iop.org/article/10.1088/1742-6596/289/1/012010/meta
40. Shpotyuk O, Filipecki J (2003) Free volume in vitreous chalcogenide semiconductors: possibilities of positron annihilation lifetime study. Wyd-wo WSP w Czestochowie, Czestochowa
41. Klym H, Ingram A (2007) Unified model of multichannel positron annihilation in nanoporous magnesium aluminate ceramics. J Phys Conf Ser 79(1):012014. http://dx.doi.org/10.1088/1742-6596/79/1/012014
42. Klym H, Karbovnyk I, Guidi MC, Hotra O, Popov AI (2016) Optical and vibrational spectra of CsCl-enriched GeS_2-Ga_2S_3 glasses. Nanoscale Res Lett 11(1):1–6. doi:10.1186/s11671-016-1350-8

43. Ingram A, Golovchak R, Kostrzewa M, Wacke S, Shpotyuk M, Shpotyuk O (2012) Compositional dependences of average positron lifetime in binary as-S/se glasses. Phys B Condens Matter 407(4):652–655. http://dx.doi.org/10.1016/j.physb.2011.11.052
44. Calvez L, Lin C, Rozé M, Ledemi Y, Guillevic E, Bureau B, Allix M, Zhang X (2010) Similar behaviors of sulfide and selenide-based chalcogenide glasses to form glass-ceramics. Proc SPIE 7598:759802-1-16. doi:10.1117/12.840968
45. Klym H, Ingram A, Shpotyuk O, Hadzaman I, Solntsev V, Hotra O, Popov AI (2016) Positron annihilation characterization of free volume in micro-and macro-modified $Cu_{0.4}Co_{0.4}Ni_{0.4}Mn_{1.8}O_4$ ceramics. Low Temperature Phys 42(7):601–605. http://dx.doi.org/10.1063/1.4959021
46. Krause-Rehberg R, Leipner HS (1999) Positron annihilation in semiconductors. Defect studies. Springer, Berlin/Heidelberg/New York, p 378
47. Klym H, Ingram A, Shpotyuk O, Filipecki J (2010) PALS as characterization tool in application to humidity-sensitive electroceramics. 27th international conference on microelectronics proceedings (MIEL). Proceedings of the 27th International Conference, pp 239–242. doi:10.1109/MIEL.2010.5490492
48. Nambissan PMG, Upadhyay C, Verma HC (2003) Positron lifetime spectroscopic studies of nanocrystalline $ZnFe_2O_4$. J Appl Phys 93:6320. http://dx.doi.org/10.1063/1.1569973
49. Leifer I, Patro RK (2002) The bubble mechanism for methane transport from the shallow sea bed to the surface: a review and sensitivity study. Cont Shelf Res 22(16):2409–2428. http://dx.doi.org/10.1016/S0278-4343(02)00065-1
50. Ljunggren S, Eriksson JC (1997) The lifetime of a colloid-sized gas bubble in water and the cause of the hydrophobic attraction. Colloids Surf A Physicochem Eng Asp 129:151–155. http://dx.doi.org/10.1016/S0927-7757(97)00033-2
51. Grosman A, Ortega C (2005) Nature of capillary condensation and evaporation processes in ordered porous materials. Langmuir 21:10515–10521. doi:10.1021/la051030o
52. Tao SJ (1972) Positronium annihilation in molecular substance. J Chem Phys 56(11):5499–5510. http://dx.doi.org/10.1063/1.1677067
53. Eldrup M, Lightbody D, Sherwood JN (1981) The temperature dependence of positron lifetimes in solid pivalic acid. Chem Phys 63:51–58. http://dx.doi.org/10.1016/0301-0104(81)80307-2